nature electronics

Article

https://doi.org/10.1038/s41928-022-00859-y

An organic artificial spiking neuron for in situ neuromorphic sensing and biointerfacing

Received: 2 March 2022

Accepted: 29 September 2022

Published online: 7 November 2022

Check for updates

Tanmoy Sarkar[1,7,8], Katharina Lieberth[1,8], Aristea Pavlou[1], Thomas Frank[2], Volker Mailaender[1,3], Iain McCulloch[4,5], Paul W. M. Blom[1], Fabrizio Torricelli[6] ✉ & Paschalis Gkoupidenis[1] ✉

The effective mimicry of neurons is key to the development of neuromorphic electronics. However, artificial neurons are not typically capable of operating in biological environments, which limits their ability to interface with biological components and to offer realistic neuronal emulation. Organic artificial neurons based on conventional circuit oscillators have been created, but they require many elements for their implementation. Here we report an organic artificial neuron that is based on a compact nonlinear electrochemical element. The artificial neuron can operate in a liquid and is sensitive to the concentration of biological species (such as dopamine or ions) in its surroundings. The system offers in situ operation and spiking behaviour in biologically relevant environments—including typical physiological and pathological concentration ranges (5–150 mM)—and with ion specificity. Small-amplitude (1–150 mV) electrochemical oscillations and noise in the electrolytic medium shape the neuronal dynamics, whereas changes in ionic (≥2% over the physiological baseline) and biomolecular (≥ 0.1 mM dopamine) concentrations modulate the neuronal excitability. We also create biohybrid interfaces in which an artificial neuron functions synergistically and in real time with epithelial cell biological membranes.

Neurons are the fundamental units of the nervous system and are used to transmit and process electrochemical signals. They operate in a liquid electrolyte and communicate with each other via gaps (synapses) between the axon of pre-synaptic neurons and the dendrite of post-synaptic neurons (Fig. 1a). Neuromorphic computing uses hardware-based implementations to mimic the behaviour of synapses and neurons[1], for efficient brain-inspired computing. The approach could also be used to interface biology with electronics that share similar biocomputational primitives[2–7]. Synaptic phenomena—the gradual and activity-dependent coupling between neurons—are typically mapped onto memory devices, which can be binary, multistate or analogue. However, to emulate neuronal spiking and oscillatory dynamics, electronic oscillatory circuitry is required[8,9].

Neuron-like dynamics can be created with conventional microelectronics using oscillatory circuit topologies to mimic neuronal behaviours. For example, neuromorphic electronic circuits consisting of ring oscillators have been used for the implementation of mechanically flexible, skin-inspired electronics and neuro-inspired mechanoreceptors[10,11]. Many-element artificial neurons based on solid-state silicon or organic devices have also been reported[9,11–13]. However, although these approaches can mimic specific aspects of neuronal behaviour, the integration of a large numbers of transistors and passive electronic

[1]Max Planck Institute for Polymer Research, Mainz, Germany. [2]Max Planck Institute of Neurobiology, Martinsried, Germany. [3]Dermatology Clinic, University Medical Center of the Johannes Gutenberg-University Mainz, Mainz, Germany. [4]KAUST Solar Center, Physical Science and Engineering Division, King Abdullah University of Science and Technology (KAUST), Thuwal, Saudi Arabia. [5]Department of Chemistry, University of Oxford, Oxford, UK. [6]Department of Information Engineering, University of Brescia, Brescia, Italy. [7]Present address: Infineon Technologies AG, Dresden, Germany. [8]These authors contributed equally: Tanmoy Sarkar, Katharina Lieberth. ✉e-mail: fabrizio.torricelli@unibs.it; gkoupidenis@mpip-mainz.mpg.de

https://doi.org/10.1038/s41928-022-00859-y

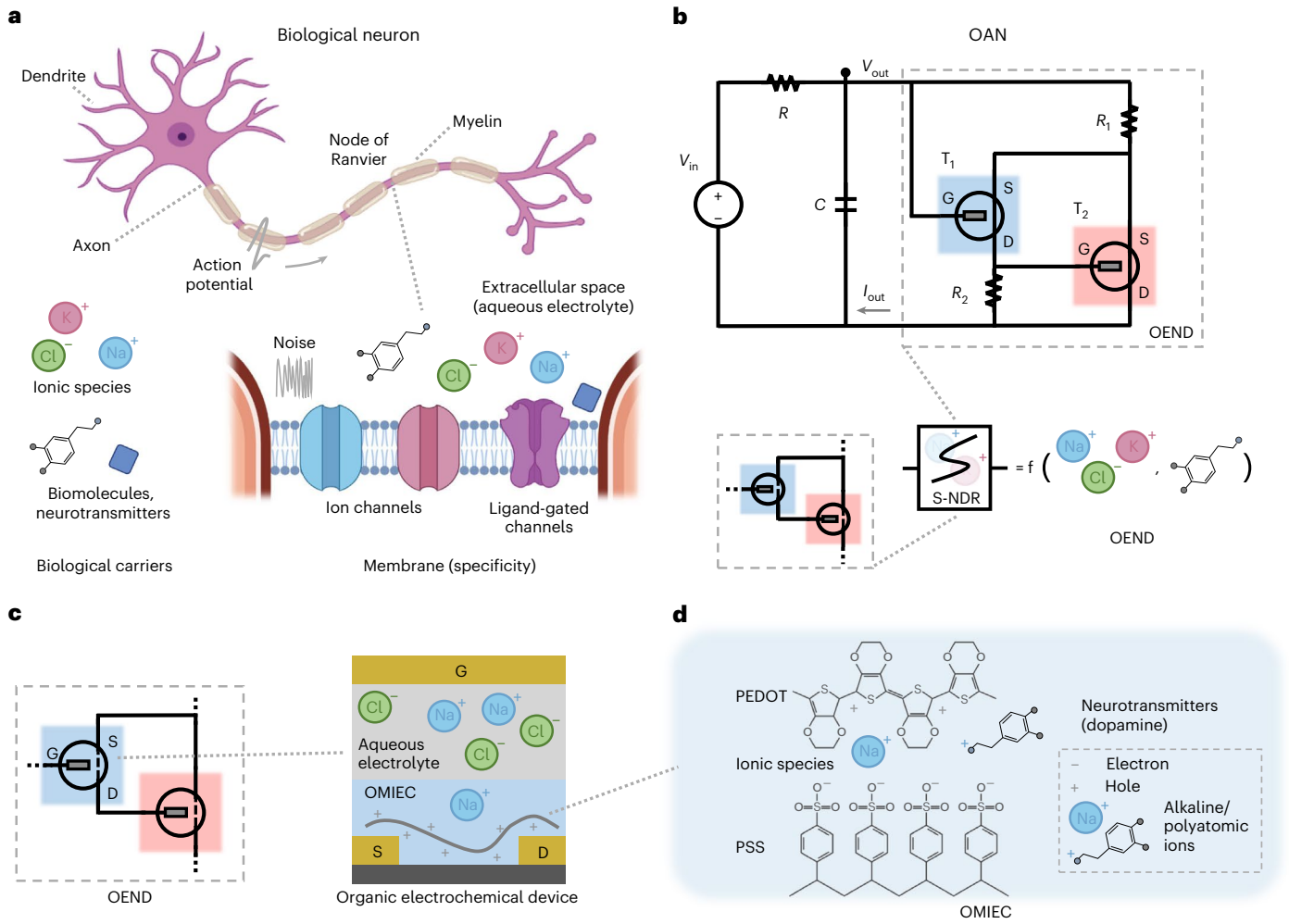

Fig. 1 | A biological neuron and the OAN. a, Simplified schematic of a biological neuron. Action potentials, the basic cell-to-cell communication events, are generated by rapid transmembrane ion exchanges through ion channels, and they propagate across the axon. In myelinated cells, alternate myelin/non-myelin domains (nodes of Ranvier) contribute to the fast and long-range action potential propagation. Biological neurons are immersed in an electrochemical environment, such as an aqueous electrolyte. This extracellular space is a common reservoir containing various biological carriers for signalling and processing (ions, biomolecules and so on). Noise is also present in this environment. Ionic channels on the membrane endow neurons with ionic/molecular specificity and recognition. **b**, Circuit diagram of the OAN. The main part is an OEND that displays S-shaped negative differential resistance (S-NDR) phenomena and is responsive to ionic and biomolecular species common to biological environments. The OEND consists of two OECTs, namely, T_1 and T_2, that are connected via the $R_1 = 5$ kΩ and $R_2 = 10$ kΩ resistors in a cascade-like configuration with feedback. The OAN is formed when the OEND is connected to an *RC* element ($R = 10$ kΩ; $C = 6$ nF to 10 μF) and voltage source V_{in}. Here V_{out} and I_{out} are the resulting output voltage and current, respectively, of the OEND under the influence of V_{in}. G, gate; S, source; D, drain. **c**, Schematic of the OECT that forms the OEND. The channel of the OECT consists of an organic mixed ionic–electronic conductor (OMIEC), such as PEDOT:PSS. **d**, Sensing mechanism in PEDOT:PSS. Ionic or polyatomic ions interact with PEDOT:PSS and modulate the doping level and hole conductivity of PEDOT:PSS, which results in a change in the OECT drain current and threshold voltage.

components results in bulky biomimetic circuits that are not suitable for direct, in situ biointerfacing.

Volatile and nonlinear devices based on memristors or spin torque oscillators can be used to increase the integration density and emulating neuronal dynamics[14,15]. Metal-oxide memristive devices based on metal–insulator transitions exhibit negative differential resistance phenomena that are suitable for the emulation of neuronal dynamics[14]. Such devices with a negative differential resistance are locally active, and therefore, electrical input stimuli trigger voltage or current spikes in analogy with biological neurons. Artificial neurons based on memristive devices with a negative differential resistance have the potential for high integration density[1,16]. Nevertheless, the intrinsic sensitivity of solid-state memristive devices to moisture prevents in situ biointerfacing in biologically relevant host environments[17]. Although memristive arrays have been used for pre- and post-acquisition biosignal processing, they have not been used for in situ biointerfacing[18,19].

Spin torque oscillators are magnetic nanodevices compatible with silicon technology[1,15]. Their nonlinearity and dynamics have been recently leveraged for spoken language and audible source recognition[15]. However, there is no viable route for biointerfacing with spin torque oscillators, as their oscillatory dynamics are too fast (around gigahertz frequencies) for interacting in real time with biological processes. Their operation also requires the presence of magnetic fields. Other approaches for spiking or oscillatory devices and circuits—including Mott-transition-based memristive devices[20,21], ferroelectrics[22], photonics[23] and two-dimensional materials[24]—have been developed, but all of them encounter similar problems. By omitting various aspects of actual biological wetware, artificial neurons based on electronics are insufficiently capable of emulating/handling the biosignal diversity and thus of operating in situ in biological environments.

Organic electrochemical devices based on organic mixed ionic–electronic conductors offer an alternative approach to neuromorphic

https://doi.org/10.1038/s41928-022-00859-y

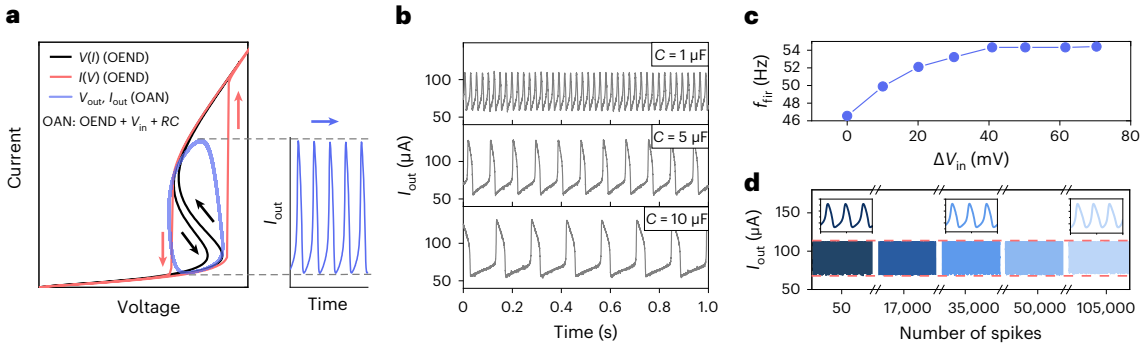

Fig. 2 | Nonlinear phenomena of the OEND and bifurcation. a, Nonlinear phenomena of the OEND in the *V*(*I*) mode (application of current sweep and measurement of the resulting voltage) and *I*(*V*) mode (application of voltage sweep and measurement of the resulting current). Parametric oscillations (Lissajous-like plot) of the OAN (OEND + V_{in} + *RC*) and their projection in the current versus time plane are shown. Here I_{out} (V_{out}) is the output current (voltage) between the OEND and (V_{in} + *RC*). **b**, Regular (tonic) current spiking I_{out} for various capacitances *C* = 1–10 μF and V_{in} = 1.75 V. The *y* axes are the same for all the subpanels. **c**, Frequency response of a voltage-controlled oscillator (*C* = 1 μF). This response shows the firing frequency versus input voltage difference (f_{fir} versus ΔV_{in}), where $\Delta V_{in} = V_{in} - V_{th}$ is the input voltage above the threshold voltage V_{th} for spiking. **d**, Continuous OAN firing under fixed V_{in}. The insets show the stability of the spiking waveform for 50, 3.5×10^4 and 1.05×10^5 spiking cycles. All the measurements are performed in an aqueous electrolyte (100 mM NaCl).

electronics[25]. Organic electronics can operate in close proximity to biology due to their soft nature and the ability to directly interact with ions in aqueous electrolytes[3,26,27]. Organic synaptic transistors have developed rapidly, showing outstanding analogue memory phenomena with low-voltage operation and linearity in weight update (in contrast, nonlinear phenomena are required for the implementation of neuronal dynamics)[28–31]. In addition, organic artificial synaptic devices have demonstrated neurotransmitter-mediated plasticity when coupled with dopaminergic cells[32,33] and have also been interfaced with non-electrogenic cells[34]. However, such devices are passive elements and therefore are not able to emulate neuronal dynamics. Recently, organic electrochemical neurons have been reported[13]. However, this approach is based on many-element conventional oscillatory circuitry and does not possess the complexity in neuronal dynamics that nonlinear elements can potentially display. The integration of neuromorphic electronics with biology requires artificial synapses that can interface with biological ones, as well as artificial spiking neurons that can operate and respond to local biological signals in situ, that is, in the wet biological environment.

In this Article, we report an organic artificial spiking neuron with electrobiochemical degrees of control that enable local and in situ neuromorphic sensing and biointerfacing. The organic artificial neuron (OAN) can operate in a liquid and shows inherent biosensing primitives. It consists of a compact nonlinear electrochemical element that exhibits negative differential resistance that is sensitive to the biological environment that hosts the OAN. The OAN responds to ionic species commonly found in the extracellular space, and its spiking response is sensitive to typical physiological and pathological ionic concentration ranges (5–150 mM). Small-amplitude (1–150 mV) electrochemical oscillations and noise in the electrolytic medium shape the neuronal firing properties. Therefore, the artificial neuron exhibits spiking properties (which are stable for $>10^5$ spiking cycles) that depend on the local ionic, biomolecular or neurotransmitter species of the aqueous environment—behaviour that is analogous to a biological neuron that is surrounded by the extracellular space containing various biological carriers for signalling and processing (Fig. 1a). In particular, in situ changes in ionic (≥2% increase) and biomolecular (≥0.1 mM of dopamine) concentrations modulate the neuronal excitability and trigger spikes. Ion-specific oscillations for sodium (Na^+) and potassium (K^+) are also possible, providing a pathway for emulating ion channel dynamics. Furthermore, we create a biohybrid interface in which artificial neurons synergistically function with membranes of epithelial cells and where the biological membrane barrier modulates the spiking properties of the artificial neuron in real time.

Organic artificial spiking neuron

The OAN consists of a compact nonlinear building block made of only two organic electrochemical transistors (OECTs), namely, T_1 and T_2 (Fig. 1b). Both OECTs are p-type transistors: T_1 is a depletion-mode transistor, whereas T_2 is an enhancement-mode transistor. The mixed ionic–electronic conductor poly(3,4-ethylenedioxythiophene) (PEDOT) doped with poly(styrene sulfonate) (PSS) and poly(2-(3,3′-bis(2-(2-(2-methoxyethoxy)ethoxy)ethoxy)-[2,2′-bithiophen]-5-yl) thieno [3,2-b] thiophene) (p(g2T-TT)) are used for the T_1 and T_2 channel, respectively[35,36]. The electrical characteristics of T_1 and T_2 are presented in Supplementary Fig. 1. The OECTs operate in aqueous environments and are sensitive to ionic species and polyatomic ions (Fig. 1c). For instance, the channel of T_1 consists of the organic mixed ionic–electronic conductor PEDOT:PSS (ref. [26]). Both channel and gate of an OECT are in direct contact with the electrolyte. In the case of a p-type OECT, when a positive gate voltage V_G is applied, cations drift into the polymeric channel and reduce the hole concentration, and consequently, drain current I_D is lowered. When a negative V_G is applied, cations are removed from and anions drift into the polymeric channel, the hole concentration increases, and this results in a larger I_D. In OECTs, ions can penetrate the bulk of the polymer and the volumetric nanoscale ionic–electronic charge compensation results in a large current modulation. This high gate voltage to drain current modulation yields a high transconductance, which is the hallmark of OECTs. Another key feature of OECTs is the dependence of I_D on the ion concentration in the electrolyte. More precisely, the fixed charges in the ion-conducting phase of the polymeric channel are electrostatically compensated by the mobile ions provided by the electrolyte. This Donnan equilibrium results in a concentration-dependent voltage drop at the polymer/electrolyte interface, which is, in turn, mirrored by the OECT threshold voltage. As shown in Fig. 1d, ionic or polyatomic cations (anions) interact with PEDOT, a hole conductor, and PSS, an ionic conductor, and decrease (increase) the doping level of PEDOT, resulting in a decrease (increase) in I_D and the OECT threshold voltage (Fig. 1d). Here T_1 and T_2 are connected in the cascade-like configuration with feedback resistors R_1 and R_2, obtaining a two-terminal organic electrochemical nonlinear device (OEND) (Fig. 1b).

The current–voltage *V*(*I*) and voltage–current *I*(*V*) characteristics of the OEND are displayed in Fig. 2a. The OEND is accessed either in the *V*(*I*) or *I*(*V*) mode with current *I* or voltage *V* as the independent variable, respectively. An S-shaped negative differential resistance is accessible only in the *V*(*I*) mode, by applying current at the single-valued negative differential resistance characteristic. In the *I*(*V*) mode, the OEND

shows multivalued characteristic with unstable points of operation to be directly accessed by applying a voltage. A detailed analysis of the OEND response with experimental and simulation data is shown in Supplementary Figs. 1 and 2. Consecutive $V(I)$ or $I(V)$ scans display highly reproducible responses of the OEND (Supplementary Fig. 3). The time response τ_{OEND} of the OEND element for square-wave input pulses is $\tau_{OEND} \approx 11$ ms (Supplementary Fig. 3).

When the OEND is coupled to an RC element (Fig. 1b) forming an OAN, its response bifurcates, producing voltage or current oscillations (Fig. 2; load-line analysis is shown in Supplementary Fig. 4). These spike-based oscillations represent the 'action potentials' of the OAN (Supplementary Fig. 5). Figure 2b displays the current response I_{out} of the OAN for different values of capacitor C. The firing frequency f_{fir} can be finely tuned between 6 and 40 Hz by changing C, a range that is consistent with physiological levels of instantaneous firing rates in biological neurons[37]. The firing frequency range can be further extended by modifying C or by using high-frequency-response OECTs[38]. In the case of polymer-based capacitors, capacitances in the range of nanofarads to microfarads can be reached with micrometre-scale PEDOT:PSS-based capacitors[26]. The parametric oscillatory response in the I–V plane and the instantaneous power dissipation P_{inst} of the OAN is shown in Supplementary Fig. 6. The instantaneous power dissipation is given by $P_{inst} = V_{in}/R(V_{in} - V_{out})$, where V_{in}, V_{out} and I_{out} refer to the input voltage, output voltage and output current of the whole OAN, respectively. The calculation includes all the OAN components (for example, transistors, resistors and capacitor). The mean power dissipation $P_{mean} = 143$ μW. As shown in Fig. 2c and Supplementary Fig. 7, the OAN behaves as a voltage-controlled oscillator and f_{fir} is modulated by increasing ΔV_{in} ($\Delta V_{in} = V_{in} - V_{th}$, where V_{th} is the OAN oscillation threshold) within the oscillation window. For $\Delta V_{in} = 0$–70 mV, the relative increase in firing frequency is $\Delta f_{fir}/f_{min} \cong 18\%$, with a voltage-controlled oscillator sensitivity of $\Delta f_{fir}/f_{min}/\Delta V_{in} \cong 260\%$ per volt.

The amplitude and window of the current or voltage oscillations can be precisely designed (Supplementary Fig. 8), for instance, by engineering the threshold voltage of transistors T_1 and T_2. In this case, the oscillatory window is shifted to a lower voltage level when decreasing the threshold voltage of T_1 by doping PEDOT:PSS with the amine-based molecular dopant N-methyl-2,2′-diaminodiethylamine (ref. [39]), and P_{mean} is decreased from 143 to 24 μW. For a capacitor with $C = 6$ nF and by neglecting the static power dissipation, the energy consumption per spike is $E_{spike} = 57$ nJ. The amplitude profile of the current oscillations can also be engineered by varying R_1 and R_2 of the OAN (the effect of R_1 and R_2 on the nonlinear properties of the OEND is shown in Supplementary Fig. 2). It should be noted that doping causes permanent threshold-voltage shifts and dynamic reconfigurability can be induced by introducing synaptic transistors instead of volatile ones. In the case of PEDOT:PSS, the threshold voltage can be tuned on the fly by changing the ion concentration[40], a phenomenon that is exploited here to obtain an ion-concentration-dependent firing frequency. The OAN displays fully consistent stability when continuously operated at various amplitude and frequency conditions, as the firing response is practically unaffected for $>10^5$ spiking cycles (Fig. 2d). The OAN stability as a function of the number of spikes is also evaluated. The amplitude of I_{out} reduces by ~2.8×10^{-5}% per spike. As a result, after 10^6 spikes, the OAN current amplitude is equal to approximately 71% of the initial amplitude.

The OAN shows the key characteristics observed in the spiking response of biological neurons. The OAN operates in a liquid, a property that is reminiscent of the extracellular environment of biological neurons in the cerebrospinal fluid. The excitability of the OAN, that is, the tendency of a neuron to fire spikes, can be modulated by the presence of electrochemical oscillations transmitted by means of ionic fluxes in the electrolytic medium. Figure 3a shows that the in-liquid electrochemical oscillations shape the firing properties of the OAN, mimicking the characteristic features of biological neurons[41]. An increase of only a few millivolts at the potential of the electrolytic medium elicits spikes with high temporal precision (Supplementary Fig. 9), and a forced bursting activity is phase locked with the ionic signal in the electrolyte. During the time window of the input signal that is above the OAN threshold voltage V_{th}, the OAN fires and therefore the input phase coordinates firing. Variation in the electrolyte potential as small as 1–2 mV at the very edge of the OAN threshold V_{th} results in stochastic firing, thus reproducing the behaviour observed in biological neurons[42]. Such small variations in the electrolytic medium potential are in the same range of the biopotentials of the extracellular electrolytic space (microvolts to millivolts)[43]. The OAN threshold allows for additional bioplausible behaviours, such as in-liquid all-or-nothing spiking and subthreshold oscillations (Supplementary Figs. 9 and 10, respectively). The spiking properties of the OAN for input voltage pulses is shown in Supplementary Fig. 9.

Due to its finite response time, the OAN displays a stimulus–response delay (Fig. 3b), as well as behaves as a temporal integrator (Fig. 3c). The stimulus–response delay in biological neurons, known as spike latency, can provide a rapid and efficient neural coding scheme beyond simple rate coding, as latency can be a faster differentiator than the mean firing rates[44]. We further investigate this delay and reproduce the spike latency characteristic of biological neurons. Figure 3b shows that the stimulus-firing phase difference $\Delta\varphi$ is modulated by the input voltage difference ΔV_{in} (time-domain response is shown in Supplementary Fig. 11). Stronger stimulation induces shorter latencies, as observed in biological sensory systems[45]. Due to the finite and relatively slow time constant of biomembranes, biological neurons temporally integrate inputs and display firing under certain interstimulus timing conditions[46]. This integration lowers the timing precision and offers temporal buffering windows for ongoing neuronal inputs, ensuring the consolidation and stability of neuronal sequences[46]. Analogous to biological neurons, the OAN integrates time, buffers input stimuli and fires for short non-overlapping interstimulus intervals (Fig. 3c).

Biological environments are characterized by seemingly random fluctuations at a range of spatiotemporal scales, and therefore, neurons are constantly operating under noisy conditions[47]. This noise couples with neuronal dynamics, influencing neuronal excitability and firing properties. Although counterintuitive, noise can be beneficial for neuronal communication and processing. For instance, noise can enable the transmission of weak subthreshold signals, smoothens subthreshold-to-threshold nonlinearities or even enhances the communication efficiency by increasing the signal-to-noise ratio or by altering the neuronal coding schemes[47]. The noise-induced activity of the OAN is presented in Fig. 3d. The OAN is biased with a d.c. input voltage at the subthreshold regime, and white noise of variable amplitude ($V_{pp} = 5$–150 mV) is injected in the electrolytic medium to emulate extracellular noise/fluctuations. As the amplitude of the noise increases, a gradual transition from tonic ($V_{pp} = 0$–25 mV) to irregular firing ($V_{pp} = 50$ mV) is observed. For low noise levels, the frequency of tonic firing remains practically constant, that is, $f_{fir} \cong 6.5$–7.0 Hz. As the noise level increases, packets of spikes are observed. Recurrence plots of the interspike intervals and spike-to-spike amplitudes (Supplementary Fig. 12) indicate a change in the coding scheme from tonic to noise-induced bursting activity, as well as the resilience of spiking against noise in the electrolytic medium.

In situ spike-based neuromorphic sensing

It is estimated that the extracellular electrolytic space occupies a volume fraction of ~15–30% of the brain tissue. This extracellular space is an aqueous electrolyte comprising various ionic species (mostly Na^+, K^+, Cl^- and Ca^{2+}) and represents a reservoir by maintaining homoeostatic balance of the ion concentrations under physiological conditions. In mammalian cells, the range of physiological concentrations for Na^+ is $c_{ext} = 130$–150 mM and $c_{int} = 10$–15 mM and for K^+, $c_{ext} = 3$–12 mM and $c_{int} = 150$–160 mM, where c_{ext} and c_{int} are the

https://doi.org/10.1038/s41928-022-00859-y

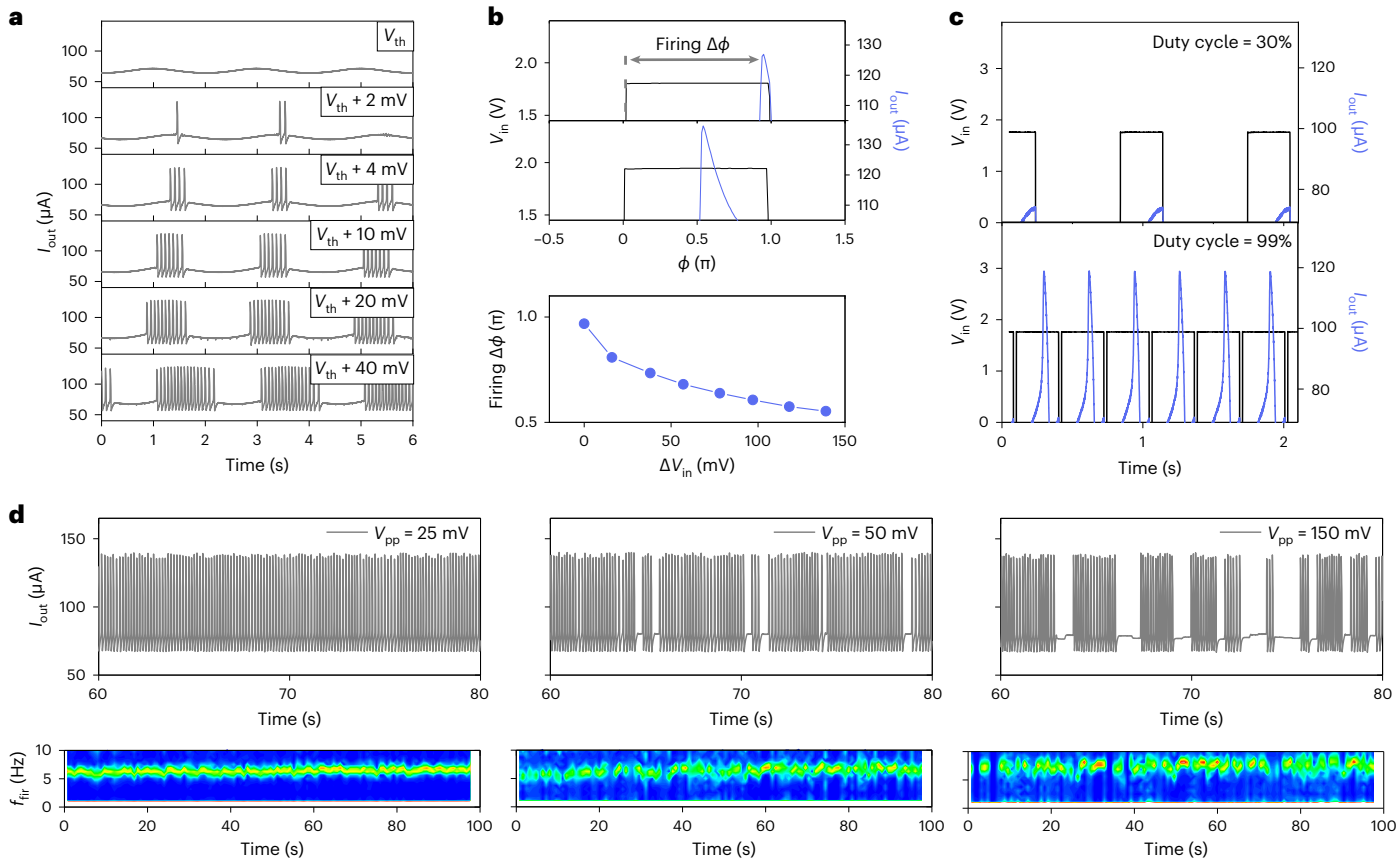

Fig. 3 | An organic artificial spiking neuron. a, Electrochemical oscillation-mediated neuronal firing. The OAN is biased with a time-varying input voltage V_{in} via the electrolytic medium of T_1 and T_2, with a d.c. bias of 1.68 V and an a.c. signal of 50 mV_{pp} ($\leq V_{th}$ of the OAN). Phase-dependent firing is observed for electrolyte voltage differences of 1–40 mV above the firing threshold V_{th}. **b**, In-liquid spike latency (firing phase delay $\Delta\varphi$ versus ΔV_{in}). **c**, In-liquid temporal integration. Firing occurs for short interstimulus time intervals or high duty cycles. **d**, Noise-induced neuronal firing of the OAN with different levels of amplitude of white noise in the electrolytic medium. I_{out} versus time (top) and the corresponding time–frequency analysis (bottom) or short-time Fourier-transform spectrogram for representative amplitudes (V_{pp} = 25, 50 and 150 mV). White noise at the electrolytic medium (V_{pp} = 5–150 mV) induces activity transition from tonic firing to bursting, with constant firing frequency $f_{fir} \approx$ 6.5–7.0 Hz. All the measurements are performed in an aqueous electrolyte (100 mM NaCl).

extracellular and intracellular concentrations, respectively[48]. Although homoeostatically balanced, these ion concentrations can change in different spatiotemporal scales. Minute concentration variations in the proximal extracellular space of a neuron are induced during an action potential (fluctuations of approximately 5% for Na^+ and 20% for K^+ from physiological baselines)[49]. Many pathological conditions (for example, spreading depression, epilepsy and migraines) are manifested as homoeostatic imbalance; for instance, extracellular Na^+ and K^+ concentrations can decrease to 60 mM and increase to roughly 55 mM, respectively[50]. Moreover, the extracellular medium contributes to intercellular, non-synaptic communication via variations in the extracellular electric fields (for example, ephaptic coupling)[51], neurotransmitter spillover (such as diffusion to adjacent synapses)[52] or via extracellular-mediated diffusion of neuromodulators[53].

The OAN, due to its in-liquid operation, exhibits firing properties that depend on the ionic concentration of the electrolyte host. As the electrolyte concentration increases, the ionic conductivity of the electrolyte also increases; thus, T_1 (or T_2) has a lower response time and f_{fir} increases[54]. Figure 4a shows the dependence of the firing waveform on the NaCl concentration (in an aqueous solution), c_{NaCl}. Here f_{fir} increases from 25 to >50 Hz for c_{NaCl} = 80–150 mM, a range that is on par with common physiological and pathological extracellular Na^+ concentrations (Fig. 4b). This results in a relative increase in the firing frequency of $\Delta f_{fir}/f_{min} \cong 110\%$ and agrees with the behaviour of biological neurons in which f_{fir} increases with the extracellular Na^+ concentration[55]. As further confirmation, Supplementary Fig. 13 shows that the OAN also operates under the common physiological/pathological range of extracellular K^+ concentrations in an aqueous solution, namely, c_{KCl} = 5–50 mM; furthermore, in this case, f_{fir} increases with the K^+ concentration. The responsiveness of the OAN at biophysically relevant ionic concentration ranges is essential for the in situ operation of the OAN with biological membranes and neurons.

Changes in ionic concentration gradients between the intracellular and extracellular medium of biological neurons alter their excitability/threshold, and firing can be initiated by varying these concentrations[56]. As an example, Fig. 4c shows that small variations (~2–10%) in NaCl concentration over a biologically relevant baseline (100 mM NaCl) can increase the OAN excitability and induce firing. Both f_{fir} and time delay between the increase in concentration and neuronal excitation Δt_{fir} correlate with the ion concentration (Supplementary Fig. 14). Moreover, the behaviour shown in Fig. 4c is in agreement with the excitation profiles for similar extracellular Na^+ concentrations of the Hodgkin–Huxley neuron model (Supplementary Fig. 14).

Dopamine is a modulatory neurotransmitter that regulates essential brain functions including cognition, learning, motivation, motor control, mood regulation and addiction[57]. At the cellular level, dopamine can impact neuronal excitability in a multitude of ways (resulting in excitatory or inhibitory and time- and concentration-dependent

https://doi.org/10.1038/s41928-022-00859-y

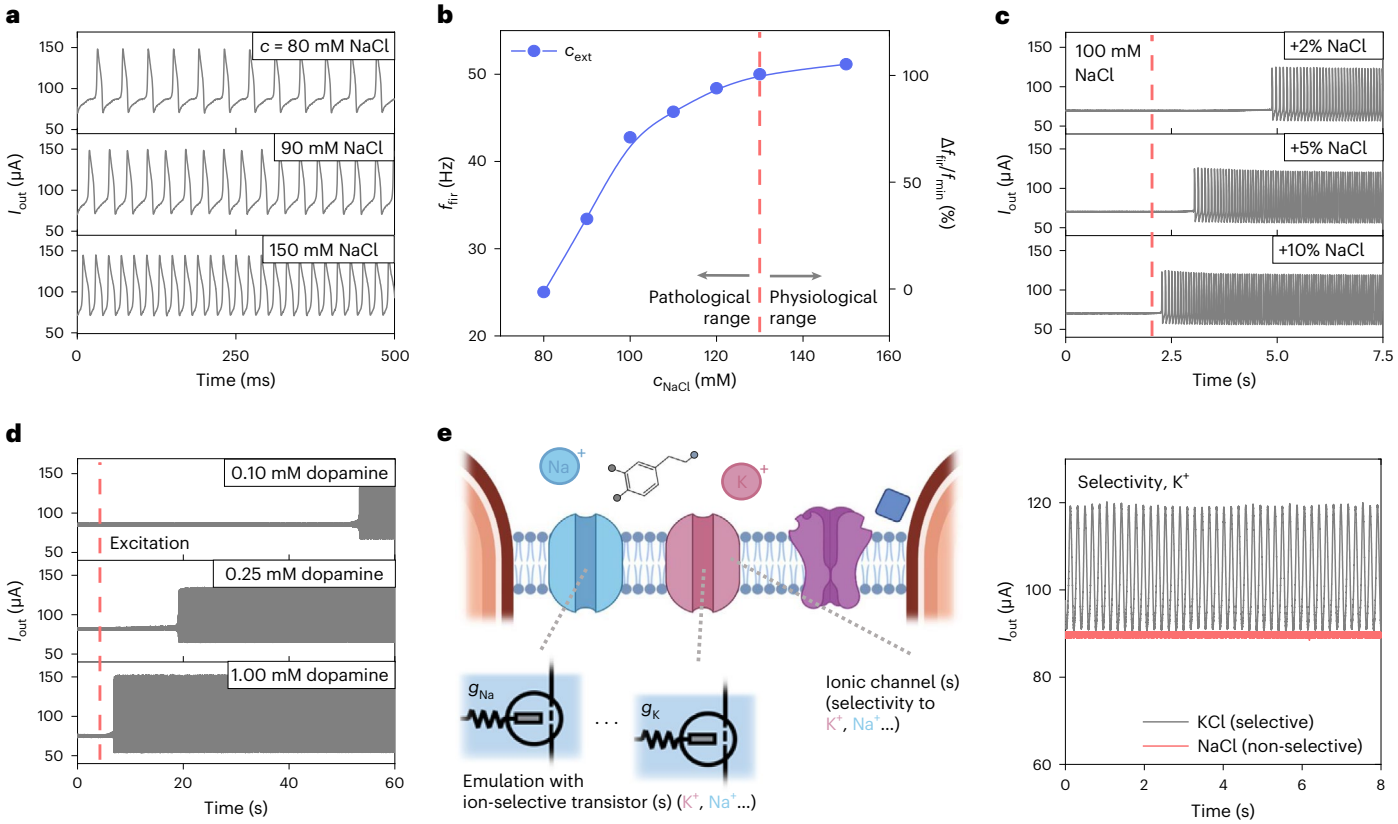

Fig. 4 | In situ spike-based neuromorphic sensing. a, Representative waveforms of the OAN firing response for different ionic concentrations (here aqueous NaCl). **b**, Electrolyte-controlled oscillators of the OAN. Firing frequency as a function of ionic concentration, f_{fir} versus c_{NaCl}. The range of extracellular Na^+ concentrations c_{ext} under common physiological and pathological conditions in the brain is indicated by the red dashed line. **c**, Electrolyte-induced excitability of the OAN. Minute perturbations in ionic concentrations (2–10% NaCl) over the physiologically relevant baseline (100 Mm NaCl) enhance the neuronal excitability and initiate tonic spiking. **d**, I_{out} as a function of time. The presence of dopamine (0.1–2.0 mM) in the cell culture solution (phosphate-buffered saline) excites the OAN and induces tonic spiking, demonstrating neurotransmitter-induced excitability. **e**, Ion-selective OANs induce ion-specific oscillations, emulating the dynamics of biological ion channels in liquid and on chip (channel conductance g_K, g_{Na}). As an example, the OAN is selective to K^+ ions and insensitive to Na^+ interfering ions. In all the experiments (ion concentration changes, exposure to dopamine and incorporation of ion-selective membranes), the sensing device is T_1 and the same electrolyte conditions (100 mM NaCl) are maintained for T_2.

effects), both via synaptic and non-synaptic activation of dopamine receptors[58]. For example, dopamine has a net excitatory effect on primate pyramidal neurons[59]. As shown in Fig. 4d, the presence of dopamine in the electrolyte increases the excitability of the OAN and initiates tonic firing. Excitation is observed in shorter time delays Δt_{fir} for higher dopamine concentrations, whereas a slight decrease in f_{fir} is observed (Supplementary Fig. 15). The behaviour shown in Fig. 4d highlights that the initiation of spikes can be biochemically triggered, a property that resembles the biological neuronal signalling phenomena. It should be noted that the OAN also exhibits biorealistic diversity in signalling, as dopamine-mediated inhibition can be induced by altering the OAN biasing scheme (Supplementary Fig. 15).

The ion channels of biological membranes pass inward and outward ionic currents, a hallmark of neuronal signalling[60]. The dysregulation of these processes is the consequence of a large number of channelopathies that can lead to serious pathological conditions such as cystic fibrosis and myotonia congenita[61]. Another layer of biophysical realism is added to the OAN response by implementing on-chip selectivity and specificity characteristics, akin to biological ion channels. Figure 4e demonstrates that the OAN function directly incorporates aspects of the molecular machinery that are responsible for the selective processing of the biological carriers of information. OANs displaying ion-specific (Na^+ or K^+) oscillatory activities are realized by incorporating ionophore-based selective membranes[62] at the channel/electrolyte interface of T_1 (Fig. 1b). As an example, a K^+-selective OAN shows oscillations in the case of the KCl electrolyte, with f_{fir} increasing with the ion-selected concentration, but does not show oscillations in a control experiment with NaCl electrolyte (Supplementary Fig. 16). The selectivity library can be further extended with membranes that are selective to other biologically relevant ions such as Na^+, Ca^{2+} and ammonium (NH_4^+) (refs. [63,64]).

Biohybrid neuron

The OAN is capable of direct biointerfacing in a biologically relevant environment, and a biohybrid neuron is formed by incorporating a biomembrane between the gate and channel of T_1 (Fig. 5). The system consists of a biological and artificial compartment. As a relevant biomembrane model system, the prototypical epithelial cell line Caco-2, which is a model of the intestinal epithelial barrier and widely used for in vitro toxicology and drug delivery studies[65–67], is incorporated with the OAN. The biomembrane comprises epithelial cells joined with tight junctions, thus forming a natural barrier for ion passage (Fig. 5a). The biohybrid neuron functions in situ and in real time (Fig. 5b). Initially, the OAN is operated in a plain cell culture medium; in the absence of the biomembrane barrier, electrochemical oscillations are sustained at $f_{fir} \cong 12$ Hz. A barrier functionality is induced with the incorporation of the biomembrane. This biomembrane barrier blocks the gate-to-channel ion passage and suppresses the oscillations of the biohybrid neuron, with $f_{fir} \cong 0$ Hz. The addition of a chemical agent that attacks the biomembrane's tight junctions—here the toxin hydrogen

https://doi.org/10.1038/s41928-022-00859-y

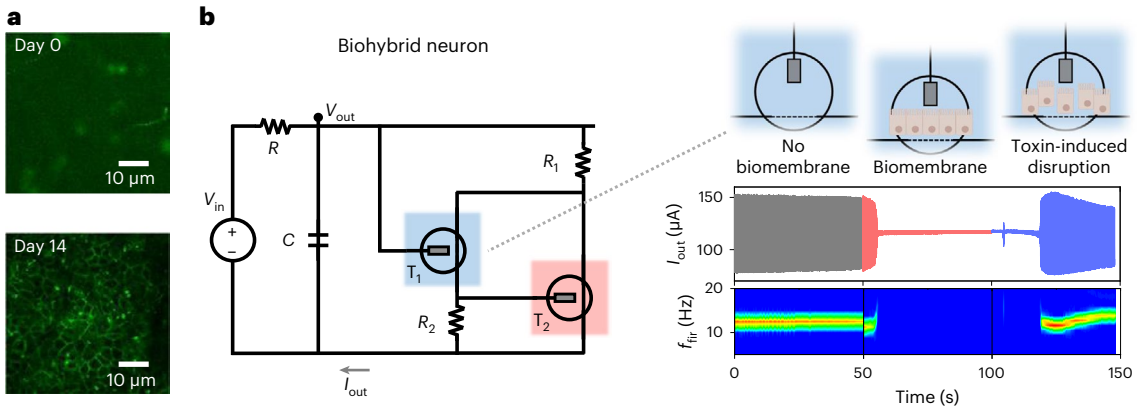

Fig. 5 | A biohybrid neuron for in situ spike-based neuromorphic biointerfacing. a, Optical microphotograph (representative of 10–15 similar experiments) of the cell culture of the Caco-2 cell line as a biomembrane model for the implementation of biohybrid neurons. Immunostaining of occludin (coloured in green) as a relevant tight junction protein confirms the barrier function of the biomembrane. Day 0 of cell culturing indicates the absence of tight junctions. Day 14 of cell culturing indicates the presence of tight junctions that form a barrier for ion passage through the biomembrane. **b**, Schematic of the biohybrid neuron consisting of an OAN with the incorporated biomembrane. I_{out} versus time and the corresponding time–frequency analysis of the biohybrid neuron is displayed. The presence of an ion-blocking epithelial biomembrane between the gate and channel of T_1 suppresses the neuronal excitability and spiking that is initially observed in the plain cell culture medium. Toxin-mediated opening of the biomembrane by attacking its tight junctions results in the recovery of the spiking activity over time. In the biohybrid neuron experiment, the sensing device is T_1 (that is, incorporation of the biomembrane) and keeping the same electrolyte conditions in T_2 (100 mM NaCl).

peroxide—lowers the barrier of ion passage and results in a gradual recovery of oscillations. This demonstration shows that the biomembrane dynamics change the excitability of the OAN in real time, and this is directly reflected on the firing response of the biohybrid neuron. A more detailed schematic of the biohybrid neuron and a description of the biomembrane disruption mechanism are shown in Supplementary Fig. 17. Such biohybrid systems can be used as controllable in vitro models for basic research, such as to understand the underlying mechanisms of neuronal signalling, as well as a platform for studying the barrier integrity of biological tissues under various physiopathological conditions or the influence of external physicochemical cues (toxins, neuromodulators and so on). It should also be mentioned that interfacing the OAN with biological neurons requires that both domains have similar dimensions. Therefore, careful design of the OAN is necessary, as the device dimensions play a critical role in the spiking response of the OAN. The impact of the device dimension on the OAN spiking response with simulations is shown in Supplementary Fig. 18.

Conclusions

We have reported an OAN based on a nonlinear electrochemical element. Inspired by the properties of biological neurons functioning in wet surroundings, the OAN can mimic the biological sensitivity to ionic and biomolecular species in a surrounding aqueous environment. The artificial neuron exhibits nonlinear phenomena that depend on the composition of biophysically relevant host environments. We experimentally validated its operation with various electrolytes, including common aqueous electrolytes, buffered solutions and cell culture media. We also created biohybrid interfaces in which the OAN was modulated by the biological membrane of epithelial cells in situ and in real time. A comparison with the state-of-the-art technology is provided in Supplementary Tables 1 and 2.

Neuronal excitability, dynamics and spiking properties depend on the electrolytic potential and noise, as well as on the local concentrations of specific ionic and biomolecular species. Therefore, just as in biological neurons—where sensing and actuation is merged and happens locally in the same surroundings—sensing (for example, neurotransmitters) and actuation/communication (via spiking, oscillating or other behaviours) are inherently embedded in the device operation, and this can enable tighter closed-loop control of biological substrates. The operation in close physical, functional and temporal proximity with biology can enable the real-time interaction between artificial and biological rhythmicity, for example, the development of new strategies for understanding, restoring and augmenting biorhythmic processes.

In contrast to conventional organic ring oscillators that consist of multiple transistors, only two transistors are required for the OAN. This compactness means that the OAN can potentially be merged into a single device—a challenging venture for many-element implementations. Negative-differential-resistance-based ionoelectronics can lead to much richer dynamics compared with conventional electronics. For practical applications, the integration density and variability of soft matter devices should be further developed and improved. In addition, although the OAN is externally powered in this work, biofuel-powered and self-sustainable oscillators could be developed that emulate certain metabolic pathways of biological neurons[68]. Non-synaptic modes of neuronal communication that are found in biological networks could be introduced with global electrolytes[69,70]. Furthermore, synaptic capabilities can be introduced at the function of the OAN circuit, by incorporating organic synaptic transistors[28,31,71,72]. Finally, in the case of dopamine detection, latent 'memory time windows' can form the basis for on-chip learning phenomena, such as biomolecular reward prediction error coding[73].

Methods

Fabrication of OENDs and OANs

Standard microscope glass slides (75 mm × 25 mm) were cleaned in a sonicated bath, first in soap solution (Micro-90 (Sigma-Aldrich)) and then in a 1:1 (vol/vol) solvent mixture of acetone and isopropanol. Gold electrodes for source and drain electrodes were photolithographically patterned (with positive Microposit S1813 photoresist (DOW)) on the cleaned glass slides. A chromium layer was used to improve the adhesion of gold. Each glass slide contains a series of circuit blocks consisting of T_1 and T_2 OECTs. The channel dimensions of T_1 and T_2 are $W_1 \times L_1 = 50\ \mu m \times 20\ \mu m$ and $W_2 \times L_2 = 50\ \mu m \times 10\ \mu m$, respectively. The OECTs are separately gated with Ag/AgCl electrodes via aqueous electrolytes. Two layers of parylene C (SCS Coatings) were deposited. Soap (Micro-90 soap solution, 1% vol/vol in deionized water) was used for separation between the parylene C layers to enable the peel-off of the upper parylene C layer. The lower parylene C layer insulates the

gold electrodes. A promoter (Silane A-174 (γ-methacryloxypropyl trimethoxysilane), Sigma-Aldrich) was added to the lower parylene C layer to enhance adhesion. In the second photolithography step using the positive photoresist AZ 9260 MicroChemicals (Cipec Spécialités), the channel dimensions of T_1 and T_2 are defined. Reactive ion etching (O_2/CF_4 plasma, 160 W for 16 min with O_2 flow rate of 50 s.c.c.m. and CHF_3 flow rate of 5 s.c.c.m.) was used to define the channels of T_1 and T_2 throughout the photoresist mask. The channel of T_1 is made with the organic mixed ionic–electronic conductor polymer PEDOT:PSS (Clevios PH 1000) mixed with 5.0 wt% ethylene glycol, 0.1 wt% dodecyl benzene sulfonic acid and 1.0 wt% (3-glycidyloxypropyl)trimethoxysilane. The film was spin coated in two steps at 1,500 rpm and 650 rpm for 1 min and annealed at 120 °C for 1 min in between. The devices were subsequently baked at 140 °C for 1 hour. For the implementation of T_2, the semiconducting polymer p(g2T-TT) was synthesized according to another work[36]. Here p(g2T-TT) was dissolved in chloroform (3 mg ml^{-1}) inside a N_2-filled glovebox and spin coated in ambient conditions at 1,000 rpm for 1 min resulting in a thickness of 40 nm. The devices were baked at 60 °C for 1 min. The sacrificial upper parylene C layer was peeled off to confine the polymer to the inside of the channel regions. Excess soap was rinsed off with deionized water. A schematic of the OAN is shown in Supplementary Fig. 19.

Electrical characterization of OENDs and OANs

The current versus voltage characteristics of the individual OECTs and OENDs were obtained using a Keithley 2400 semiconductor parameter analyser. Ag/AgCl were used as the gate electrodes with 100 mM NaCl electrolyte solution, unless otherwise stated. The nonlinear characteristics of the OENDs were obtained by enforcing current when the corresponding voltage was measured or by enforcing voltage when the corresponding current was measured. The OEND was coupled with *RC* and V_{in} elements (external components) to complete the OAN, which exhibits neuronal dynamics when connected to voltage source V_{in} (Fig. 1b). The voltage oscillation was directly recorded at the V_{out} terminal using an Agilent infiniiVision digital oscilloscope. The output current I_{out} of the OEND is measured by measuring the voltage V_0 across resistor R_M with a differential amplifier (based on an INA122 integrated circuit) and a digital oscilloscope (Supplementary Fig. 20). To characterize the OAN response in the presence of different electrobiochemical signals, a Tektronix AFG1022 arbitrary function generator was used for the input voltage. The arbitrary function generator and semiconductor parameter analyser were used together to generate an arbitrary noise signal for the noise-induced neuronal characterization, phase-locking measurements and characterization of the various neuromorphic behaviours. The spectrogram of the short-time Fourier transform was performed using OriginPro 2016 with a Hanning-type window.

Data availability

The data that support the findings of this study are available from the corresponding authors on reasonable request. Source data are provided with this paper.

References

1. Zhang, W. et al. Neuro-inspired computing chips. *Nat. Electron.* **3**, 371–382 (2020).
2. Vassanelli, S. & Mahmud, M. Trends and challenges in neuroengineering: toward 'intelligent' neuroprostheses through brain-'brain inspired systems' communication. *Front. Neurosci.* **10**, 438 (2016).
3. van de Burgt, Y. & Gkoupidenis, P. Organic materials and devices for brain-inspired computing: from artificial implementation to biophysical realism. *MRS Bull.* **45**, 631–640 (2020).
4. Ham, D., Park, H., Hwang, S. & Kim, K. Neuromorphic electronics based on copying and pasting the brain. *Nat. Electron.* **4**, 635–644 (2021).
5. Mikhaylov, A. et al. Neurohybrid memristive CMOS-integrated systems for biosensors and neuroprosthetics. *Front. Neurosci.* **14**, 358 (2020).
6. Shchanikov, S. et al. Designing a bidirectional, adaptive neural interface incorporating machine learning capabilities and memristor-enhanced hardware. *Chaos Solit. Fractals* **142**, 110504 (2021).
7. Serb, A. et al. Memristive synapses connect brain and silicon spiking neurons. *Sci. Rep.* **10**, 2590 (2020).
8. Marković, D., Mizrahi, A., Querlioz, D. & Grollier, J. Physics for neuromorphic computing. *Nat. Rev. Phys.* **2**, 499–510 (2020).
9. Indiveri, G. et al. Neuromorphic silicon neuron circuits. *Front. Neurosci.* **5**, 73 (2011).
10. Tee, B. C.-K. et al. A skin-inspired organic digital mechanoreceptor. *Science* **350**, 313–316 (2015).
11. Mirshojaeian Hosseini, M. J. et al. Organic electronics Axon-Hillock neuromorphic circuit: towards biologically compatible, and physically flexible, integrate-and-fire spiking neural networks. *J. Phys. D: Appl. Phys.* **54**, 104004 (2020).
12. Abu-Hassan, K. et al. Optimal solid state neurons. *Nat. Commun.* **10**, 5309 (2019).
13. Harikesh, P. C. et al. Organic electrochemical neurons and synapses with ion mediated spiking. *Nat. Commun.* **13**, 901 (2022).
14. Pickett, M. D., Medeiros-Ribeiro, G. & Williams, R. S. A scalable neuristor built with Mott memristors. *Nat. Mater.* **12**, 114–117 (2013).
15. Torrejon, J. et al. Neuromorphic computing with nanoscale spintronic oscillators. *Nature* **547**, 428–431 (2017).
16. Kumar, S., Williams, R. S. & Wang, Z. Third-order nanocircuit elements for neuromorphic engineering. *Nature* **585**, 518–523 (2020).
17. Valov, I. & Tsuruoka, T. Effects of moisture and redox reactions in VCM and ECM resistive switching memories. *J. Phys. D: Appl. Phys.* **51**, 413001 (2018).
18. Gupta, I. et al. Real-time encoding and compression of neuronal spikes by metal-oxide memristors. *Nat. Commun.* **7**, 12805 (2016).
19. Liu, Z. et al. Multichannel parallel processing of neural signals in memristor arrays. *Sci. Adv.* **6**, eabc4797 (2020).
20. Zhang, X. et al. An artificial spiking afferent nerve based on Mott memristors for neurorobotics. *Nat. Commun.* **11**, 51 (2020).
21. Park, S.-O., Jeong, H., Park, J., Bae, J. & Choi, S. Experimental demonstration of highly reliable dynamic memristor for artificial neuron and neuromorphic computing. *Nat. Commun.* **13**, 2888 (2022).
22. Mulaosmanovic, H., Chicca, E., Bertele, M., Mikolajick, T. & Slesazeck, S. Mimicking biological neurons with a nanoscale ferroelectric transistor. *Nanoscale* **10**, 21755–21763 (2018).
23. Inagaki, T. et al. Collective and synchronous dynamics of photonic spiking neurons. *Nat. Commun.* **12**, 2325 (2021).
24. Hao, S. et al. A monolayer leaky integrate-and-fire neuron for 2D memristive neuromorphic networks. *Adv. Electron. Mater.* **6**, 1901335 (2020).
25. Ling, H. et al. Electrolyte-gated transistors for synaptic electronics, neuromorphic computing, and adaptable biointerfacing. *Appl. Phys. Rev.* **7**, 011307 (2020).
26. Rivnay, J. et al. Organic electrochemical transistors. *Nat. Rev. Mater.* **3**, 17086 (2018).
27. Cucchi, M. et al. Reservoir computing with biocompatible organic electrochemical networks for brain-inspired biosignal classification. *Sci. Adv.* **7**, eabh0693 (2021).
28. van de Burgt, Y. et al. A non-volatile organic electrochemical device as a low-voltage artificial synapse for neuromorphic computing. *Nat. Mater.* **16**, 414–418 (2017).
29. Fuller, E. J. et al. Parallel programming of an ionic floating-gate memory array for scalable neuromorphic computing. *Science* **364**, 570–574 (2019).

30. Alibart, F. et al. An organic nanoparticle transistor behaving as a biological spiking synapse. *Adv. Funct. Mater.* **20**, 330–337 (2010).
31. Gkoupidenis, P., Schaefer, N., Strakosas, X., Fairfield, J. A. & Malliaras, G. G. Synaptic plasticity functions in an organic electrochemical transistor. *Appl. Phys. Lett.* **107**, 263302 (2015).
32. Desbief, S. et al. Electrolyte-gated organic synapse transistor interfaced with neurons. *Org. Electron.* **38**, 21–28 (2016).
33. Keene, S. T. et al. A biohybrid synapse with neurotransmitter-mediated plasticity. *Nat. Mater.* **19**, 969–973 (2020).
34. Tarabella, G. et al. A hybrid living/organic electrochemical transistor based on the *Physarum polycephalum* cell endowed with both sensing and memristive properties. *Chem. Sci.* **6**, 2859–2868 (2015).
35. Bernards, D. A. & Malliaras, G. G. Steady-state and transient behavior of organic electrochemical transistors. *Adv. Funct. Mater.* **17**, 3538–3544 (2007).
36. Giovannitti, A. et al. Controlling the mode of operation of organic transistors through side-chain engineering. *Proc. Natl Acad. Sci. USA* **113**, 12017–12022 (2016).
37. Koch, C. *Biophysics of Computation: Information Processing in Single Neurons* (Oxford Univ. Press, 2020).
38. Spyropoulos, G. D., Gelinas, J. N. & Khodagholy, D. Internal ion-gated organic electrochemical transistor: a building block for integrated bioelectronics. *Sci. Adv.* **5**, eaau7378 (2019).
39. Keene, S. T. et al. Enhancement-mode PEDOT:PSS organic electrochemical transistors using molecular de-doping. *Adv. Mater.* **32**, 2000270 (2020).
40. Romele, P. et al. Multiscale real time and high sensitivity ion detection with complementary organic electrochemical transistors amplifier. *Nat. Commun.* **11**, 3743 (2020).
41. Tatsuki, F. et al. Involvement of Ca^{2+}-dependent hyperpolarization in sleep duration in mammals. *Neuron* **90**, 70–85 (2016).
42. Longtin, A. Mechanisms of stochastic phase locking. *Chaos* **5**, 209–215 (1995).
43. Buzsáki, G., Anastassiou, C. A. & Koch, C. The origin of extracellular fields and currents—EEG, ECoG, LFP and spikes. *Nat. Rev. Neurosci.* **13**, 407–420 (2012).
44. Gollisch, T. & Meister, M. Rapid neural coding in the retina with relative spike latencies. *Science* **319**, 1108–1111 (2008).
45. Gawne, T. J., Kjaer, T. W. & Richmond, B. J. Latency: another potential code for feature binding in striate cortex. *J. Neurophysiol.* **76**, 1356–1360 (1996).
46. Wutz, A., Muschter, E., van Koningsbruggen, M. G., Weisz, N. & Melcher, D. Temporal integration windows in neural processing and perception aligned to saccadic eye movements. *Curr. Biol.* **26**, 1659–1668 (2016).
47. Faisal, A. A., Selen, L. P. J. & Wolpert, D. M. Noise in the nervous system. *Nat. Rev. Neurosci.* **9**, 292–303 (2008).
48. Somjen, G. G. *Ions in the Brain: Normal Function, Seizures, and Stroke* (Oxford Univ. Press, 2004).
49. Halnes, G. et al. Effect of ionic diffusion on extracellular potentials in neural tissue. *PLoS Comput. Biol.* **12**, e1005193 (2016).
50. Hansen, A. J. & Zeuthen, T. Extracellular ion concentrations during spreading depression and ischemia in the rat brain cortex. *Acta Physiol. Scand.* **113**, 437–445 (1981).
51. Anastassiou, C. A., Perin, R., Markram, H. & Koch, C. Ephaptic coupling of cortical neurons. *Nat. Neurosci.* **14**, 217–223 (2011).
52. Nishiyama, H. & Linden, D. J. Pure spillover transmission between neurons. *Nat. Neurosci.* **10**, 675–677 (2007).
53. Syková, E. & Nicholson, C. Diffusion in brain extracellular space. *Physiol. Rev.* **88**, 1277–1340 (2008).
54. Koutsouras, D. A. et al. An iontronic multiplexer based on spatiotemporal dynamics of multiterminal organic electrochemical transistors. *Adv. Funct. Mater.* **31**, 2011013 (2021).
55. Hodgkin, A. L. & Katz, B. The effect of sodium ions on the electrical activity of giant axon of the squid. *J. Physiol.* **108**, 37–77 (1949).
56. Arakaki, X. et al. Extracellular sodium modulates the excitability of cultured hippocampal pyramidal cells. *Brain Res.* **1401**, 85–94 (2011).
57. Björklund, A. & Dunnett, S. B. Fifty years of dopamine research. *Trends Neurosci.* **30**, 185–187 (2007).
58. Seamans, J. K. & Yang, C. R. The principal features and mechanisms of dopamine modulation in the prefrontal cortex. *Prog. Neurobiol.* **74**, 1–58 (2004).
59. Henze, D. A., González-Burgos, G. R., Urban, N. N., Lewis, D. A. & Barrionuevo, G. Dopamine increases excitability of pyramidal neurons in primate prefrontal cortex. *J. Neurophysiol.* **84**, 2799–2809 (2000).
60. Kandel, E. *Principles of Neural Science* (McGraw Hill, 2021).
61. Kass, R. S. The channelopathies: novel insights into molecular and genetic mechanisms of human disease. *J. Clin. Invest.* **115**, 1986–1989 (2005).
62. Sessolo, M., Rivnay, J., Bandiello, E., Malliaras, G. G. & Bolink, H. J. Ion-selective organic electrochemical transistors. *Adv. Mater.* **26**, 4803–4807 (2014).
63. Koutsouras, D. A., Lieberth, K., Torricelli, F., Gkoupidenis, P. & Blom, P. W. M. Selective ion detection with integrated organic electrochemical transistors. *Adv. Mater. Technol.* **6**, 2100591 (2021).
64. Keene, S. T. et al. Wearable organic electrochemical transistor patch for multiplexed sensing of calcium and ammonium ions from human perspiration. *Adv. Healthcare Mater.* **8**, 1901321 (2019).
65. Sambuy, Y. et al. The Caco-2 cell line as a model of the intestinal barrier: influence of cell and culture-related factors on Caco-2 cell functional characteristics. *Cell Biol. Toxicol.* **21**, 1–26 (2005).
66. Jimison, L. H. et al. Measurement of barrier tissue integrity with an organic electrochemical transistor. *Adv. Mater.* **24**, 5919–5923 (2012).
67. Lieberth, K. et al. Monitoring reversible tight junction modulation with a current-driven organic electrochemical transistor. *Adv. Mater. Technol.* **6**, 2000940 (2021).
68. Ohayon, D. et al. Biofuel powered glucose detection in bodily fluids with an n-type conjugated polymer. *Nat. Mater.* **19**, 456–463 (2020).
69. Gkoupidenis, P., Koutsouras, D. A. & Malliaras, G. G. Neuromorphic device architectures with global connectivity through electrolyte gating. *Nat. Commun.* **8**, 15448 (2017).
70. Koutsouras, D. A., Prodromakis, T., Malliaras, G. G., Blom, P. W. M. & Gkoupidenis, P. Functional connectivity of organic neuromorphic devices by global voltage oscillations. *Adv. Intell. Syst.* **1**, 1900013 (2019).
71. Gkoupidenis, P., Schaefer, N., Garlan, B. & Malliaras, G. G. Neuromorphic functions in PEDOT:PSS organic electrochemical transistors. *Adv. Mater.* **27**, 7176–7180 (2015).
72. Yamamoto, S., Polyravas, A. G., Han, S. & Malliaras, G. G. Correlation between transient response and neuromorphic behavior in organic electrochemical transistors. *Adv. Electron. Mater.* **8**, 2101186 (2022).
73. Glimcher, P. W. Understanding dopamine and reinforcement learning: the dopamine reward prediction error hypothesis. *Proc. Natl Acad. Sci. USA* **108**, 15647–15654 (2011).

Acknowledgements

We acknowledge A. Steinmetz, A. Becker, I. Krauhausen, D. Koutsouras, H. Ling, C. Bauer and M. Beuchel from MPI for Polymer Research (MPIP) for their valuable assistance. We also acknowledge E. van Dormele from the TU Eindhoven, A. Ascoli and R. Tetzlaff from

the TU Dresden and D. Khodagholy from Columbia University for their valuable feedback. This work was performed at the facilities of MPIP (cleanroom, device metrology, electronics and mechanical workshop), which are supported by the Max Planck Society. T.S., P.W.M.B. and P.G. acknowledge funding from the Carl Zeiss Foundation via the Emergent AI Center of JGU Mainz.

Author contributions

T.S., F.T. and P.G. conceived the project, designed the experiments and analysed the data. T.S., K.L., A.P. and P.G. fabricated and characterized the OENDs and OANs. T.S., K.L., A.P. and P.G. investigated the materials and tuned their properties. I.M. designed and provided the semiconducting material(s). K.L., A.P. and V.M. provided the biomembranes. K.L., A.P. and T.S. performed the biological experiments. P.G. and F.T. performed the simulations and modelling. F.T., T.F. and P.G. prepared the manuscript with input from all the authors. P.W.M.B. and P.G. acquired the financial support.

Funding

Open access funding provided by Max Planck Society.

Competing interests

The authors declare no competing interests.

Additional information

Supplementary information The online version contains supplementary material available at https://doi.org/10.1038/s41928-022-00859-y.

Correspondence and requests for materials should be addressed to Fabrizio Torriccelli or Paschalis Gkoupidenis.

Peer review information *Nature Electronics* thanks Ming Liu, Robert Nawrocki and Sergey Shchanikov for their contribution to the peer review of this work.